Missouri University of Science and Technology
Scholars' Mine

Physics Faculty Research & Creative Works

Physics

01 Jan 2023

Realizing the Heteromorphic Superlattice: Repeated Heterolayers of Amorphous Insulator and Polycrystalline Semiconductor with Minimal Interface Defects

Woongkyu Lee

Xianyu Chen

Qing Shao

Sung Il Baik

et. al. For a complete list of authors, see https://scholarsmine.mst.edu/phys_facwork/2304

Follow this and additional works at: https://scholarsmine.mst.edu/phys_facwork

Part of the Physics Commons

Recommended Citation

W. Lee and X. Chen and Q. Shao and S. I. Baik and S. Kim and D. Seidman and M. Bedzyk and V. Dravid and J. B. Ketterson and J. E. Medvedeva and R. P. Chang and M. A. Grayson, "Realizing the Heteromorphic Superlattice: Repeated Heterolayers of Amorphous Insulator and Polycrystalline Semiconductor with Minimal Interface Defects," *Advanced Materials*, Wiley, Jan 2023.
The definitive version is available at https://doi.org/10.1002/adma.202207927

This Article - Journal is brought to you for free and open access by Scholars' Mine. It has been accepted for inclusion in Physics Faculty Research & Creative Works by an authorized administrator of Scholars' Mine. This work is protected by U. S. Copyright Law. Unauthorized use including reproduction for redistribution requires the permission of the copyright holder. For more information, please contact scholarsmine@mst.edu.

ADVANCED MATERIALS
www.advmat.de

Check for updates

Realizing the Heteromorphic Superlattice: Repeated Heterolayers of Amorphous Insulator and Polycrystalline Semiconductor with Minimal Interface Defects

Woongkyu Lee, Xianyu Chen, Qing Shao, Sung-Il Baik, Sungkyu Kim, David Seidman, Michael Bedzyk, Vinayak Dravid, John B. Ketterson, Julia Medvedeva,* Robert P. H. Chang, and Matthew A. Grayson**

An unconventional "heteromorphic" superlattice (HSL) is realized, comprised of repeated layers of different materials with differing morphologies: semiconducting *pc*-In_2O_3 layers interleaved with insulating *a*-MoO_3 layers. Originally proposed by Tsu in 1989, yet never fully realized, the high quality of the HSL heterostructure demonstrated here validates the intuition of Tsu, whereby the flexibility of the bond angle in the amorphous phase and the passivation effect of the oxide at interfacial bonds serve to create smooth, high-mobility interfaces. The alternating amorphous layers prevent strain accumulation in the polycrystalline layers while suppressing defect propagation across the HSL. For the HSL with 7:7 nm layer thickness, the observed electron mobility of 71 $cm^2 Vs^{-1}$, matches that of the highest quality In_2O_3 thin films. The atomic structure and electronic properties of crystalline In_2O_3/amorphous MoO_3 interfaces are verified using ab-initio molecular dynamics simulations and hybrid functional calculations. This work generalizes the superlattice concept to an entirely new paradigm of morphological combinations.

1. Introduction

The original introduction of heteroepitaxial superlattices with crystalline morphology by Leo Esaki and Raphael Tsu in 1970[1] laid the foundation for many modern materials breakthroughs such as the enhancement of electron mobility with modulation doping,[2] the observation of Bloch oscillations,[3] the invention of quantum cascade lasers,[4] and more recently, polar interfaces in oxide heterostructures which lead to emergent order for spin, charge, and orbital degrees of freedom[5] including superconductivity.[6] Lesser known is a follow-up proposal by Raphael Tsu in 1989[7] to further generalize the superlattice concept by growing repeated layers of different materials with different morphologies – one polycrystalline (*pc*), one amorphous (*a*) – thereby bestowing the functional advantages of superlattices to an even broader class of materials combinations. Here the name "heteromorphic superlattice" (HSL) is used to designate different material layers with different morphologies, in contrast with the term polymorphic[8] which refers to the same stoichiometric material in different phases. With heuristic arguments, Tsu proposed that the interface chemistry of the amorphous component would

W. Lee,[+] X. Chen, S.-I. Baik, S. Kim, D. Seidman, M. Bedzyk, V. Dravid, R. P. H. Chang
Department of Materials Science and Engineering
Northwestern University
Evanston, IL 60208, USA
E-mail: woong@ssu.ac.kr

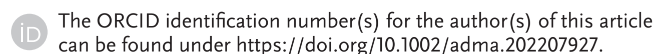
The ORCID identification number(s) for the author(s) of this article can be found under https://doi.org/10.1002/adma.202207927.

© 2023 The Authors. Advanced Materials published by Wiley-VCH GmbH. This is an open access article under the terms of the Creative Commons Attribution-NonCommercial-NoDerivs License, which permits use and distribution in any medium, provided the original work is properly cited, the use is non-commercial and no modifications or adaptations are made.

[+]Present address: Department of Materials Science and Engineering, Soongsil University, 369 Sangdo-ro, Dongjak-gu, Seoul 06978, Republic of Korea

DOI: 10.1002/adma.202207927

Q. Shao, M. A. Grayson
Department of Electrical and Computer Engineering
Northwestern University
Evanston, IL 60208, USA
E-mail: m-grayson@northwestern.edu

M. Bedzyk, J. B. Ketterson
Department of Physics and Astronomy
Northwestern University
Evanston, IL 60208, USA

J. Medvedeva
Department of Physics
Missouri University of Science and Technology
Rolla, MO 65409, USA
E-mail: juliaem@mst.edu

 © 2023 The Authors. Advanced Materials published by Wiley-VCH GmbH

allow both greater freedom of bond angles at the interface to reduce strain and greater bond passivation of the polycrystalline component to eliminate dangling bonds, thereby leading to reduced defect density and high electron mobility with "grain boundaries effectively passivated by amorphous materials."[1] However, the original attempts to realize even a single period of this structure with the polycrystalline / amorphous paring of *pc*-Si/*a*-SiO_2 yielded only semiconducting quantum dots embedded within a single oxide layer,[9] and subsequent attempts yielded only highly insulating structures,[10,11,12] leaving Tsu's original prediction of a semiconducting SL unsatisfied.

Tsu's proposition was subsequently joined with a large body of work on single heterointerfaces between (poly)crystalline and amorphous phases, where a majority focused on passivation of dangling bonds at the interface with extrinsic hydrogen,[13] but only a rare few attempted amorphous/crystalline multilayers. Interestingly, none of these HSL structures were directly deposited, but instead realized via layer-selective phase transitions. Heterolayer superlattices that were initially grown as purely crystalline underwent a layer-selective phase transition to amorphous via electrical or optical excitation or thermal annealing,[14] via irradiation by high-energy ion beams,[15] or via selective etching.[16] Or heterolayers initially grown as purely amorphous underwent layer-selective phase transition to crystalline via thermal annealing.[17,18,19] One particularly creative approach rolled up a single amorphous/crystalline heterolayer on a sacrificial strain layer to achieve a radial superlattice.[20] However, as mentioned previously, none of these structures were as-grown mixed-morphology HSLs, and none of these works tested Tsu's original proposal that the bond-angle flexibility at the intrinsic amorphous interface could serve to passivate dangling bonds.

The present paper uses precision sub-monolayer pulsed laser deposition (PLD) to demonstrate the successful fabrication of a Tsu HSL by choosing oxide compounds for each layer which have different morphologies under the same growth conditions: the polycrystalline semiconducting oxide *pc*-In_2O_3 as the "well" layer and the amorphous insulating oxide *a*-MoO_3 as the "barrier" layer. The *pc*-In_2O_3 is chosen as a representative high-mobility oxide to give electrical sensitivity to the interface quality, and the *a*-MoO_3 is chosen since its crystalline form would already permit strain relief via sliding of 2D Van der Waals layers,[21,22,23] and its amorphous form might be expected just as compliant. And whereas standard heteroepitaxy that maintains lattice periodicity can accumulate strain-induced defects with increasing SL periods,[24,25,26,27,28,29] the HSL structure would inherently relax strain within each period, with polycrystalline layers thinner than the critical thickness for defect formation interrupted by strain-relieving alternate amorphous layers.[3] The high quality of the interfaces is demonstrated with electron microscopy and X-ray spectroscopy, and high electron mobility is verified in electrical transport. To bolster the intuition in Tsu's original paper,[1] ab-initio molecular dynamics and hybrid functional calculations are performed to model the interface between crystalline In_2O_3 and amorphous MoO_3. These studies corroborate Tsu's original intuition that the relaxation of the bond angles and passivation of dangling bonds at the interface result in reduced defect density and, in turn, contribute to the experimentally observed high electron mobilities.

2. Results and Discussion

2.1. HSL Fabrication

The alternating heteromorphic units of polycrystalline-semiconducting and amorphous-insulating layers are seen in the left-side schematic of **Figure 1**a. The material choices for HSLs can, in principle, range from semiconductors to magnetic materials and superconductors. As an example, the present study employs polycrystalline semiconducting In_2O_3 and amorphous insulating MoO_3 grown via PLD (Figure S1), whereby the layer thicknesses of the HSL structures can be controlled to sub-monolayer precision. These materials are chosen since alternate layers of highly crystalline In_2O_3 and amorphous MoO_3 can both be deposited with highly reproducible properties at identical growth temperatures and oxygen partial pressures of T_g = 200 °C and P_{O2} = 15 mTorr, to assure full oxidation and minimum defects, with all other deposition parameters fixed. With the crystallization temperature of In_2O_3 at T_1 = 25 °C for crystalline fraction >80% for 350 nm films,[30] and crystallization temperature of MoO_3 at T_2 = 300 °C, the growth temperature T_g satisfies $T_1 < T_g < T_2$. As a result, with the calibrated PLD system, the HSL can be grown by simply switching between the two laser targets, MoO_3 and In_2O_3.

2.2. *pc*-In_2O_3 / *a*-MoO_3 Interface Characterization in HSL

Maintaining a sharp growth interface throughout the whole HSL up to the final deposition layer is crucial for proper realization of an HSL. To evaluate the interface quality of the fabricated HSL, high-resolution cross-sectional TEM, scanning TEM, XRD, XRR, and AFM analyses are carried out. Note that the total layer thickness of the diagnostic structures considered here (circa 350 nm) may be thicker than necessary for typical devices, but the purpose here is to demonstrate the ability to achieve smooth multilayers even in excess of standard thicknesses.

Figure 1a shows a layer schematic of HSL and a scanning TEM image of a 16-period HSL consisting of 7 nm *pc*-In_2O_3/15 nm *a*-MoO_3, where the brighter lines correspond to the In_2O_3 layer. Note the layers remain parallel throughout the structure with sharp boundaries. The left side of Figure 1b shows the higher-magnification bright-field TEM image of an equivalent HSL. The sharp interfaces between *pc*-In_2O_3 and *a*-MoO_3, have roughness much less than a nanometer. The right side of Figure 1b demonstrates growth of *a*-MoO_3 layers as thin as 0.5 nm between In_2O_3 polycrystalline layers. The sharpness of the *pc*-In_2O_3 / *a*-MoO_3 interface can also be observed from the X-ray reflectance of Figure 1c, which shows the XRR of a HSL sample with the same structure as in Figure 1a. Despite the complex structure of the HSL and the large number of layers, the XRR data can be fitted with a high-precision model using MOTOFIT software,[31] as depicted by the red line in the same graph. This fit is able to yield the average thickness of each layer, as well as the average X-ray scattering length density, from which the mass density of each layer can be calculated[32,33] with knowledge of the ideal bulk scattering length density values of In_2O_3 and MoO_3.[34] The results for the In_2O_3

© 2023 The Authors. Advanced Materials published by Wiley-VCH GmbH

15214095, 0, Downloaded from https://onlinelibrary.wiley.com/doi/10.1002/adma.202207927 by Missouri University Of Science, Wiley Online Library on [17/04/2023]. See the Terms and Conditions (https://onlinelibrary.wiley.com/terms-and-conditions) on Wiley Online Library for rules of use; OA articles are governed by the applicable Creative Commons License

15214095, 0, Downloaded from https://onlinelibrary.wiley.com/doi/10.1002/adma.202207927 by Missouri University Of Science, Wiley Online Library on [17/04/2023]. See the Terms and Conditions (https://onlinelibrary.wiley.com/terms-and-conditions) on Wiley Online Library for rules of use; OA articles are governed by the applicable Creative Commons License

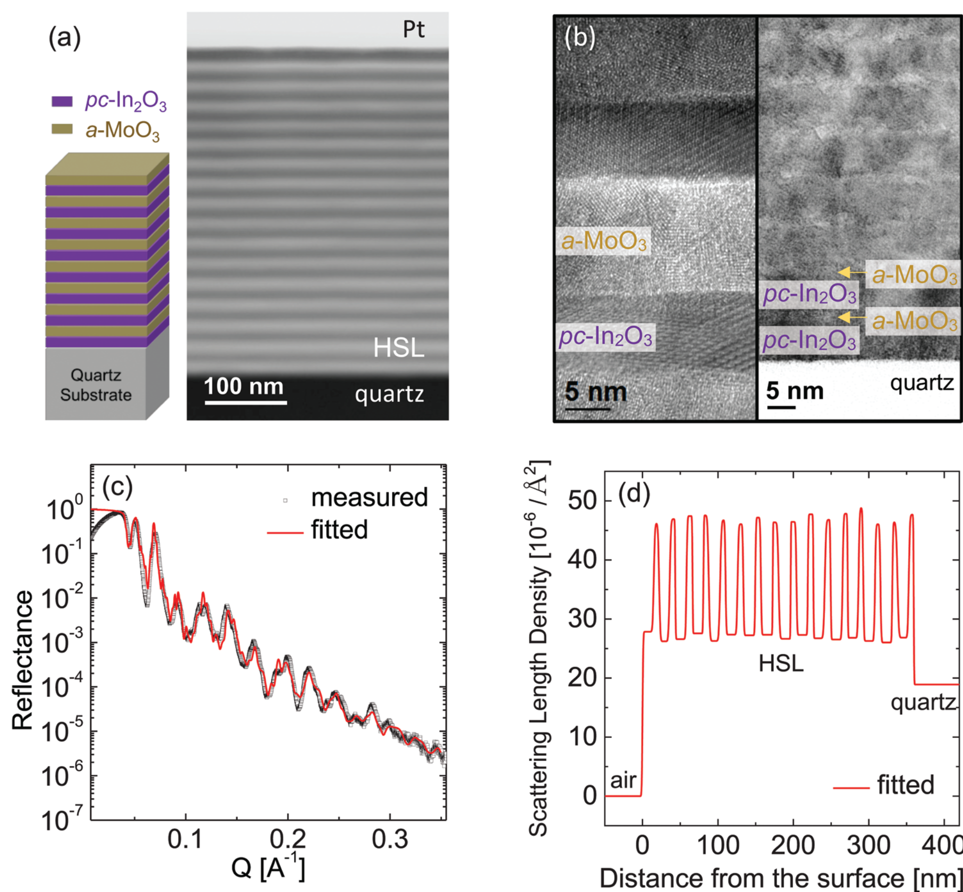

Figure 1. Physical structure of the HSL films. a) Cross-sectional scanning TEM image of a 16-bilayer HSL (7 nm *pc*-In_2O_3 / 15 nm *a*-MoO_3) on a quartz substrate. Inset: HSL schematic. b) Bright-field high-resolution TEM image of the equivalent sample (left panel) and image of a 16-bilayer HSL (7 nm *pc*-In_2O_3 / 0.5 nm *a*-MoO_3) (right panel). The Pt capping layer is adopted to protect the sample. c) XRR data and the fitted model showing remarkable agreement in the fine structure of HSL. d) The scattering length density profile is obtained from the XRR fitting of the data in (c).

layers (with ± indicating standard deviation) are an average thickness of 7.2 ± 0.5 nm, average scattering length density of $47.0 \times 10^{-6} \pm 0.8 \times 10^{-6}$ Å^{-2}), and density of 6.28 ± 0.11 g cm^{-3}. For *a*-MoO_3, the average layer thickness is 15.3 ± 0.6 nm, the average scattering length density is $26.8 \times 10^{-6} \pm 0.5 \times 10^{-6}$ Å^{-2}, and the mass density is 3.43 ± 0.06 g cm^{-3}. From these results, the In_2O_3 and MoO_3 layers have mass density ratios of 87.5% and 73.2% relative to the ideal bulk values (In_2O_3: 7.18 g cm^{-3}, MoO_3: 4.69 g cm^{-3}).[35,36] In addition, the average roughness of the interfaces is about 0.9 nm, which is consistent with that seen in Figure 1b. The variations of scattering density, roughness, and thickness of each layer from the surface down to the substrate obtained by the simulation of Figure 1c are depicted in Figure 1d. The raw values of the fit for Figure 1d are shown in Table S1 (Supporting Information). The scattering length density and thickness of the same material layers are thus very uniform, and the interfaces between layers are sharp and distinct. The growth rates of In_2O_3 and MoO_3 are calculated to be 0.233 ± 0.009 and 0.333 ± 0.023 Å/pulse, respectively, by the thickness of the XRR fitting result of Figure 1d. To confirm the growth rate of each material, 100 nm In_2O_3 and 100 nm MoO_3 single layers are grown individually on different quartz substrates. The measured thicknesses are identical, irrespective of the analysis tools as shown in Figure S2 (Supporting Information).

The AFM images in **Figure 2** indicate the film surface roughness of *pc*-In_2O_3 and *a*-MoO_3, respectively, as a function of deposition temperature, and verify the atomically smooth surface at the growth temperature of 150–250 °C. The minimal surface roughness of both the topmost *pc*-In_2O_3 layers in Figures 2a-c and, alternately, the topmost *a*-MoO_3 layers in Figures 2d–f of the HSL sample despite the overall SL thickness of 350 nm verifies the sharpness of the interfaces observed in Figure 1.

2.3. Crystalline Versus Amorphous Order of In_2O_3 and MoO_3 Layers, Respectively

To verify the HSL morphology, the crystalline or amorphous nature of the respective layers must be carefully examined and validated.[1] Thus the selective area diffraction patterns (SADPs) from TEM and high-resolution XRD analyses are examined.

Figure 3a shows the SADPs obtained from the sample. The magnification is controlled so that the whole multilayer oxide region is sampled in the SADP image. The diffraction spots marked by the purple arrows "a" and "b", indicate In_2O_3 features which match well with the (222) and (211) planes, respectively, of the cubic (bixbyite, space group of Ia-3) structure of In_2O_3. (Ref: ICDD 00-006-0416) It is noted that many diffraction patterns,

© 2023 The Authors. Advanced Materials published by Wiley-VCH GmbH

15214095, 0, Downloaded from https://onlinelibrary.wiley.com/doi/10.1002/adma.202207927 by Missouri University Of Science, Wiley Online Library on [17/04/2023]. See the Terms and Conditions (https://onlinelibrary.wiley.com/terms-and-conditions) on Wiley Online Library for rules of use; OA articles are governed by the applicable Creative Commons License

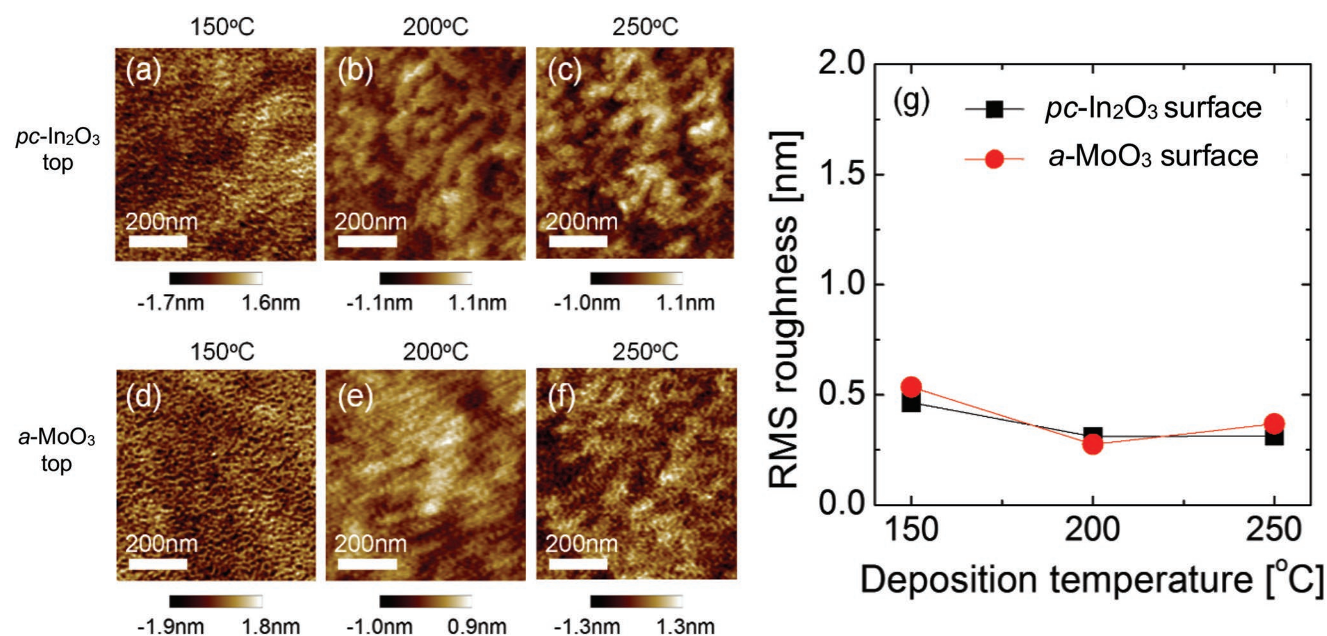

Figure 2. Surface morphology of pc-In_2O_3 and a-MoO_3 layers. The AFM topographic images of the top 7 nm pc-In_2O_3 layer of 16 bilayers (7 nm pc-In_2O_3/15 nm a-MoO_3) deposited at a) 150 °C, b) 200 °C, and c) 250 °C, respectively. The AFM topographic images of the top a-MoO_3 layer similarly atop 16 bilayers grown at d) 150 °C, e) 200 °C, and f) 250 °C, respectively. g) The summary of the RMS surface roughness obtained from (a–f) implies extremely sharp interfaces throughout.

especially the "a" spots, are positioned at the top side of the transmitted electron beam. This implies that the sample has strong (222)-texture in the multilayer growth direction. This corroborates the XRD results in Figure 3b which also shows high preferred orientation of the (222) plane. The amorphous ring indicated by the gold arrow "c" indicates lack of long-range order in the pure amorphous MoO_3 layer grown at these temperatures.

Figure 3b shows the theta-2 theta XRD patterns of a 280-nm-thick In_2O_3 single layer, a 7 nm pc-In_2O_3 / 15 nm a-MoO_3 HSL consisting of ×16 bilayers (with a total thickness of 352 nm), a 400-nm-thick MoO_3 single layer on a fused quartz substrate, and finally a fused quartz substrate with no deposition. The broad feature around 22° is seen to result from the fused quartz substrate, alone. In the single layer In_2O_3 (purple), a very sharp and intense peak from the (222) plane appears at around 30.1° as well as peaks from the (211), (400), (332), (431), (440), (622), and (444) planes, with calibrated crystalline planes from ICDD 00-006-0416 marked with vertical lines. Although the HSL had high (222)-preferred orientation, the Laue oscillations were hard to observe due to the small nonunifomity of repeated bilayers in the HSL. From the SEM image (Figure S3, Supporting Information), the thick In_2O_3 is observed to grow in a continuous columnar mode with circa 20 nm diameter columns.[37] Compared to the reference In_2O_3 peak positions shown as vertical gray lines in Figure 3b, every peak of the 280-nm-thick In_2O_3 is shifted to the lower angle, indicating residual compressive in-plane strain. However, the XRD peak positions of the HSL sample are better aligned with the unstrained bulk In_2O_3 reference peak positions, indicating that no residual strain is present in the HSL. This suggests the critical role of the alternating layers of crystalline and amorphous films in relieving strain in the polycrystalline layer.

Finally, the slightly enhanced linewidth in Figure 3b of the In_2O_3 peaks in the HSL structure (red) compared to the columnar crystalline layer (purple) indicates greater inhomogeneity of the In_2O_3 layer within the HSL. Since higher-order peaks are not sufficiently resolved, a Williamson-Hall[38] type analysis cannot distinguish the source of the inhomogeneity, but it can put an upper limit on any possible strain inhomogeneity and a lower limit on typical crystal grain size. The result is a maximum strain inhomogeneity of $\Delta E = 0.006$ for the In_2O_3 single layer and 0.016 for the In_2O_3 layer in the HSL, or, alternatively, a minimum limit of $\delta x = 22.22$ nm average crystallite size for the In_2O_3 single layer and 8.2 nm for the In_2O_3 layer in the HSL. We note that the 22.2 nm limit for In_2O_3 is consistent with the approximate horizontal grain size seen in Figure S3 (Supporting Information). Since the In_2O_3 single layer was grown in columnar mode, the vertical grain size, corresponding to the extracted crystallite size by XRD, was expected to be similar to or larger than the horizontal grain size. The calculated 8.2 nm crystallite size is consistent with the HSL In_2O_3 layer thickness of 7 nm, thus, the crystal grain size, alone, seems to account for the diffraction peak broadening, aside from any consideration of strain.

2.4. HSL Enhancement of Electron Mobility

Mobility and electron density are two sensitive indicators of defects as they are both affected by interface charge traps and dangling bonds, while mobility also provides a measure of polycrystalline grain boundary scattering. Thus, the electron transport properties of the semiconducting pc-In_2O_3 layer should be an excellent indicator of growth and interface quality. Following

 © 2023 The Authors. Advanced Materials published by Wiley-VCH GmbH

15214095, 0, Downloaded from https://onlinelibrary.wiley.com/doi/10.1002/adma.202207927 by Missouri University Of Science, Wiley Online Library on [17/04/2023]. See the Terms and Conditions (https://onlinelibrary.wiley.com/terms-and-conditions) on Wiley Online Library for rules of use; OA articles are governed by the applicable Creative Commons License

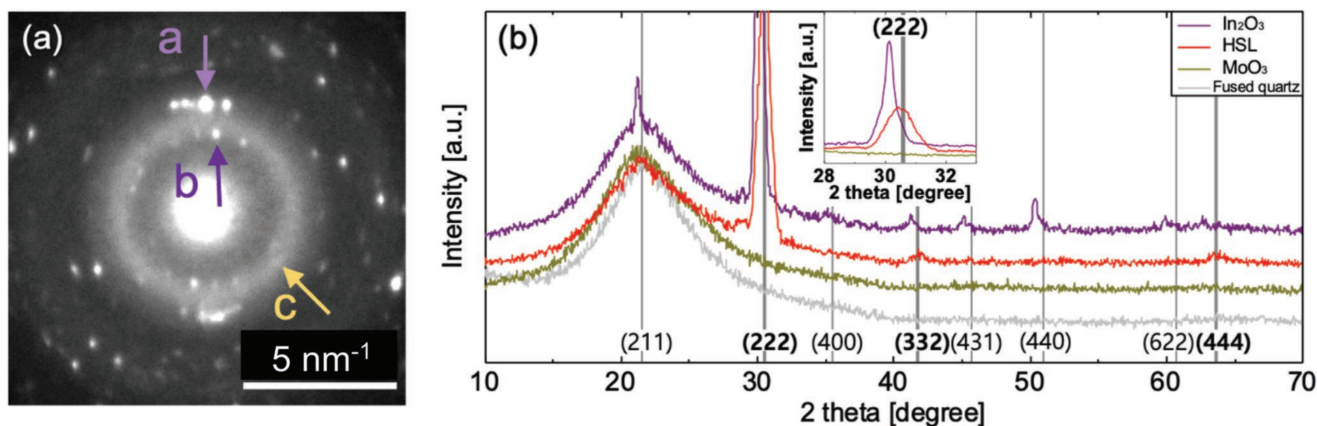

Figure 3. Crystallinity of the HSL films. a) Selective area diffraction patterns (SADP) of the entire 16-layer 7 nm *pc*-In_2O_3 / 15 nm *a*-MoO_3 HSL by TEM. Diffraction spots "a" and "b" for In_2O_3 and the diffraction ring "c" for MoO_3 are described in the text. b) Theta-2 theta XRD patterns of 280 nm In_2O_3 single layer (purple), 352 nm HSL (red), and 400 nm MoO_3 single layer (gold). The fused quartz substrate (grey) is responsible for the wide amorphous peak at 22° near the (211) line of In_2O_3. The inset in (b) shows an enlargement in 2-theta range of 28–33° around the vertical gray lines of In_2O_3 crystalline planes from ICDD 00-006-0416, where a small compressive strain is observed as a left shift of the In_2O_3 polycrystalline layer peak (purple) from the pure bulk crystal (222) plane (vertical grey line), whereas the HSL (red) exhibits no net strain, staying centered around this (222) unstrained diffraction peak. The broadening of the HSL In_2O_3 peak (red) by comparing its full width at half-maximum (FWHM) to the polycrystalline In_2O_3 peak (purple) suggests grain inhomogeneity in the HSL. The lack of any diffraction peaks whatsoever for the pure MoO_3 layer (gold), by contrast, indicates its amorphous structure at this growth temperature.

standard methods, mobility for a series of HSL samples is characterized by conducting Hall effect measurements to estimate the free electron density, then measuring the sheet conductance with the Van der Pauw method to deduce the Hall mobility. The total film thickness of circa 350 nm for each sample is confirmed with spectral reflectometry, and the doping is confirmed to be *n*-type for every sample. For comparison, the 280 nm-thick pure In_2O_3 film from the prior section was measured to establish the baseline mobility and density of pure polycrystalline In_2O_3, namely 7 $cm^2\ Vs^{-1}$. And the 400 nm-thick MoO_3 film from the prior section was confirmed to be highly insulating ($\rho > 10^5\ \Omega$cm) eliminating the need to consider parallel conduction in these layers.

The resulting mobilities and carrier densities are shown in **Figure 4**. For the samples indicated in purple, the respective layer thicknesses x were kept equal, In_2O_3:MoO_3 = x:x [nm], revealing in Figure 4a a maximum mobility of 71 $cm^2\ Vs^{-1}$ at 7:7 [nm] layer thickness. For the samples indicated in gold, the layer thicknesses maintain the In_2O_3 layer at this optimal value of 7 nm and the MoO_3 layer thickness y was varied In_2O_3:MoO_3 = 7:y [nm], and again a clear maximum is observed in Figure 4a when both layers are 7 nm thick. Note that all HSL mobilities exceed that of the pure In_2O_3 sample, indicated with the gold arrow at $y = 0$. The peak electron mobility observed here is consistent with the best mobility in In_2O_3 thin films from prior work.[12] The fact that these layers conduct at all, offers compelling evidence in favor of Tsu's intuition that the HSL is able to effectively passivate the SL interfaces without inducing high densities of dangling bonds that might trap free electron charge density and thereby reduce or eliminate conduction. On top of this, the fact that the mobility in all HSLs is consistently better than that of the bulk *pc*-In_2O_3 film implies that any density of charge traps at the interface likewise does not contribute significantly to ionized impurity scattering. On the contrary, the regular interruptions of the *a*-MoO_3 layer in the HSL structure appear to reduce the density of defects, causing mobility enhancement up to an order of magnitude relative to polycrystalline bulk, matching the highest mobility reported thus far for In_2O_3 thin films.[16] To the right of Figure 4a, the mobility drops again as the In_2O_3 layer thickness becomes larger, signifying a possible susceptibility to more grain boundary construction in thicker layers.

Further analysis of the HSL transport can place an upper bound on the number of interfacial charge traps. Figure 4b summarizes the charge density in the In_2O_3:MoO_3 = x:x [nm] samples, each of which has a 50% volume composition of In_2O_3 and therefore about half the average electron density as the pure In_2O_3 sample (purple dashed line). This observation, itself, provides evidence that the current is uniformly distributed among all layers. The proximity of the measured densities scattered around this dashed line indicates that the electron density is dominated by this bulk volume doping. Any extra doping or charge trapping at interfaces would cause a deviation from this bulk horizontal line with a sloped line proportional to the number of interfaces N, with positive slope indicating donor doping and negative slope indicating acceptor traps. A trend toward positive donor-like interface defects is noted with the grey dashed line representing an upper limit of $7 \times 10^{12}\ cm^{-2}$ charge defects per interface up to $N = 80$ interfaces per 350 nm, which abruptly turns to a high density of acceptor-like traps at $N = 100$ interfaces per 350 nm. However, below $N = 80$, the bulk doping clearly dominates, including in the optimal 7:7 nm structure. This ability to quantify the relatively low 2D density of interface defects indicates an effective passivation of dangling bonds at the interface, as predicted by Tsu. In this case, the interfaces appear to act like mild donors, slightly enhancing the free carrier density instead of inducing charge traps such as those that rendered the original attempts at Si/SiO_2 HSLs to be purely insulating.[20,21,22]

 © 2023 The Authors. Advanced Materials published by Wiley-VCH GmbH

15214095, 0, Downloaded from https://onlinelibrary.wiley.com/doi/10.1002/adma.202207927 by Missouri University Of Science, Wiley Online Library on [17/04/2023]. See the Terms and Conditions (https://onlinelibrary.wiley.com/terms-and-conditions) on Wiley Online Library for rules of use; OA articles are governed by the applicable Creative Commons License

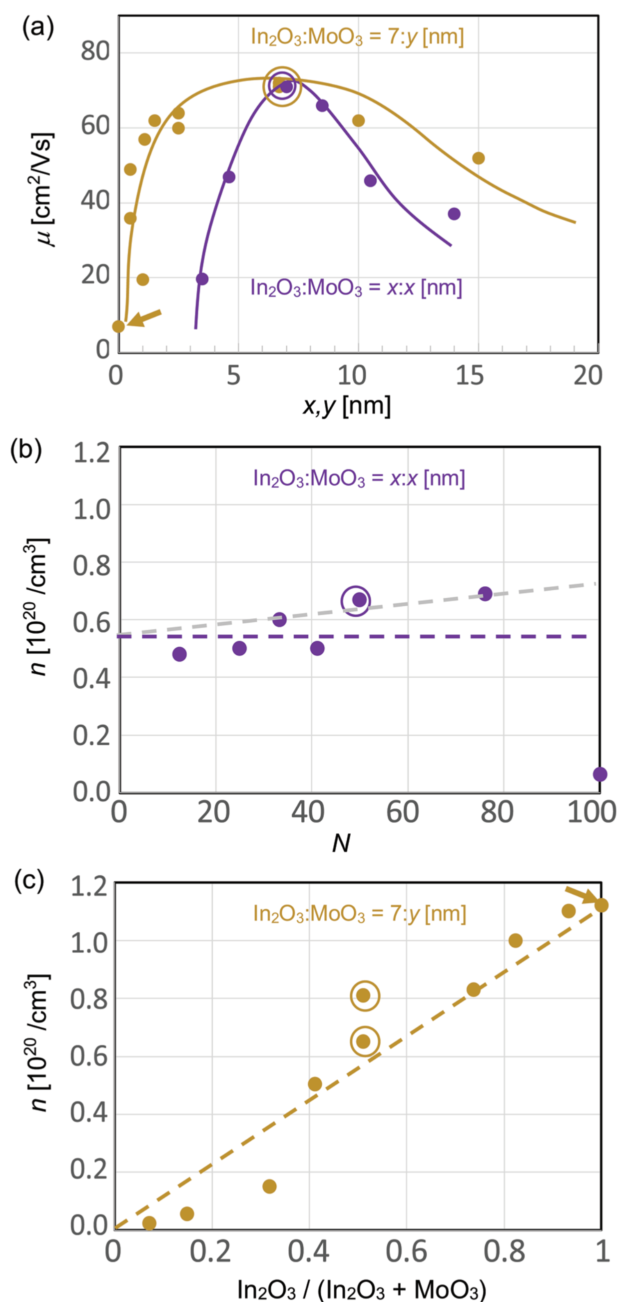

Figure 4. Optimal mobility in HSL films. Various HSLs are grown to find the optimal mobility structure. a) First, a sequence of SL periods with equal layer thicknesses of In_2O_3:MoO_3 = *x*:*x* [nm] (purple filled circles) is grown. Then a In_2O_3:MoO_3 = 7:*y* [nm] SL sequence is grown where the In_2O_3 layer thickness is held at 7 nm and the MoO_3 layer thickness is varied (gold filled circles). Lines are guides to the eye. The peak mobility of $\mu = 71$ cm^2 Vs^{-1} is observed for both sets of SLs at 7:7 nm (purple and gold open circles) and is about an order of magnitude larger than the pure In_2O_3 polycrystalline layer at *x*,*y* = 0 (gold arrow). All superlattices have total thickness around 350 nm. b) The electron density *n* of the balanced In_2O_3:MoO_3 = *x*:*x* [nm] superlattices is shown relative to the number of SL interfaces *N* per 350 nm growth. All superlattices have 50% In_2O_3 volume content and therefore about half the average electron density of a pure *pc*-In_2O_3 layer (horizontal dashed line). Only the extreme case of *N* = 100 interfaces per 350 nm SL at *x*:*x* = 3.5:3.5 nm deviates strongly from this expected average. The grey dashed line indicates a speculative 2D interface donor density of order 7×10^{12}/cm^2 setting an approximate upper bound for the interface donor charge. The open circle indicates the optimal mobility sample in this series. c) The electron density *n* of the In_2O_3:MoO_3 = 7:*y* [nm] superlattices with varying MoO_3 thickness are shown versus In_2O_3 volume fraction. The approximate agreement with the gold dashed line indicates once again that the electron density is dominated by bulk doping proportional to the In_2O_3 volume fraction. Again, the open circles indicate the optimal mobility samples in this series, and the gold arrow designates the bulk In_2O_3 sample with electron density 1.1×10^{20}/cm^3.

Finally, the dependence of electron density on relative In_2O_3:MoO_3 layer thickness is shown in Figure 4c, where the In_2O_3 thickness is kept at 7 nm and the MoO_3 thickness is varied, with pure In_2O_3 indicated in the upper right with a gold arrow. The average volume concentration of electrons in the HSL decreases monotonically with the In_2O_3 volume fraction. For In_2O_3 volume fractions above 40%, the electron density is clearly proportional to the In_2O_3 volume fraction, consistent with the dominant In_2O_3 bulk doping assumption as indicated by the diagonal dashed line, with the high mobility 7:7 nm HSL structure indicated with a gold circle.

2.5. Theoretical Calculations of Crystalline In_2O_3/Amorphous MoO_3 Interface

To complement experimental evidence of Tsu's heteromorphic interface model, the structural properties of the stoichiometric *c*-In_2O_3/*a*-MoO_3 interface are investigated using ab-initio MD simulations and accurate hybrid functional calculations. Given the limitations on the size of the simulated supercell, the *pc*-In_2O_3 is approximated as a single crystalline grain in a unit SL supercell with periodic boundary conditions. In **Figure 5**a, the atomic structure of one realization of the stoichiometric *c*-In_2O_3/*a*-MoO_3 model with superlattice layers of approximately 10:10 Å is depicted. Following Tsu,[1] one critical factor for growing HSL structures is the preservation of the stoichiometry. Therefore, in Figure 5b, the effective coordination numbers of individual In and Mo atoms are calculated, plotted as a function of the *z*-coordinate of the atom across the interface, and compared to the average value in the stoichiometric *c*-In_2O_3 bulk and *a*-MoO_3 bulk, respectively. The results reveal that the majority of Mo atoms within the Mo-O layer (84%) have the effective coordination at or above the bulk value, so that the Mo-O coordination averaged over the total 85 Mo atoms among 5 different interfacial models of the HSL structure is slightly higher (4.0) than the average Mo-O coordination in stoichiometric bulk (3.7). The lowest Mo-O coordination is 3.13, which is still higher than the lowest Mo-O coordination in *a*-MoO_3 bulk, 3.02. On the contrary, all except one In atom out of 160 total, have the effective coordination at or below that of the *c*-In_2O_3 bulk value (5.8). It is worthwhile to note that the coordination of 5.0 is lowest for the In-O layers nearest to the Mo-O interface at $z = 10$ Å and 20 Å, and the coordination of 5.5 is highest for the In-O layer furthest from the Mo-O interface at $z = 15$ Å. This suggests that the In atoms near the interface decrease their coordination to help maintain the stoichiometry of the amorphous Mo-O layer. At the same time, In

© 2023 The Authors. Advanced Materials published by Wiley-VCH GmbH

15214095, 0, Downloaded from https://onlinelibrary.wiley.com/doi/10.1002/adma.202207927 by Missouri University Of Science, Wiley Online Library on [17/04/2023]. See the Terms and Conditions (https://onlinelibrary.wiley.com/terms-and-conditions) on Wiley Online Library for rules of use; OA articles are governed by the applicable Creative Commons License

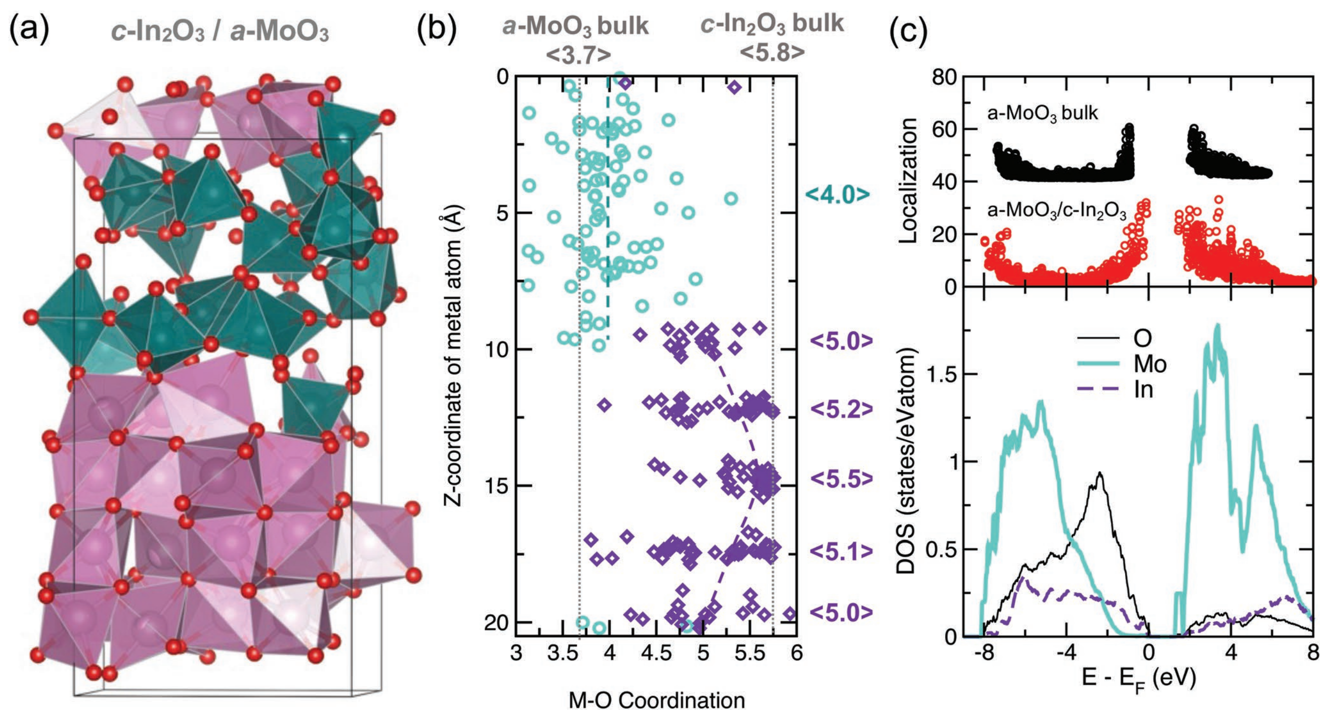

Figure 5. Ab-initio calculation of HSL. a) Example unit cell of stoichiometric monocrystalline c-In_2O_3/a-MoO_3 interface modeled via ab-initio MD simulations, with periodic boundary conditions. Purple and teal polyhedra represent In-O or Mo-O, respectively, and oxygen atoms are shown as small red spheres. b) The calculated effective coordination of the metal (M = Mo, In) with O atoms is plotted as a function of the z-coordinate of the metal atom across the interface made of stoichiometric In_2O_3/MoO_3. Every value in the plot is an average of over 3,000 MD steps at 300 K (equilibration step); the results for five independent 147-atom models of the interface are shown. Dashed teal and purple lines represent the average Mo-O and In-O coordination within a specific z-layer, respectively, with values listed to the right in angle brackets. Vertical dotted lines represent the M-O coordination values for bulk a-MoO_3 (left) and bulk c-In_2O_3 (right). (c) The electronic structure of the c-In_2O_3/a-MoO_3 interface using hybrid functional approach. The upper panel shows the inverse participation ratio representing the degree of electron localization for each state for the a-MoO_3 bulk (black) compared to the c-In_2O_3/a-MoO_3 (red). The lower panel shows the calculated density of states for O, Mo, and In states at the c-In_2O_3/a-MoO_3 interface of the HSL.

coordination recovers to the bulk value within a few atomic layers – in accord with the experimentally observed sharp interfacial region in the HSL structures, as seen in SEM micrographs above. This result confirms Tsu's intuition that the presence of an oxide at the interface helps to passivate dangling bonds, where in this case the passivating O tends to be drawn more from the In-O layer.

Proceeding with Tsu's conjecture, the angle distributions for O-M-O and M-O-M angles for M = In and/or Mo in the interfacial models were calculated and compared to the results for the corresponding bulk, see Figure S4 (Supporting Information). It is found that both O-In-O and In-O-M (M = In or Mo) angle distributions calculated for the In atoms in the a-MoO_3/c-In_2O_3 interface become broader with the major peaks reduced by about a half of the original heights in the crystalline In_2O_3. In contrast, the O-Mo-O angle distribution varies only slightly, whereas the Mo-O-M angle distribution shifts toward smaller angle values with a notable peak developed at the angle of 100°. This signifies that the internal angles within the Mo-O polyhedra are maintained upon the formation of the interface, however, the polyhedra morphology adjusts to the presence of In_2O_3, with the O-In-O angles being more compliant. Again, Tsu's intuition is confirmed, in that one characteristic of the HSL interface appears to be tolerance to bond-angle distortion, though in this case, it is the crystalline layer close to its crystallization temperature which appears to be more tolerant of bond angle distortion rather than the amorphous layer as predicted by Tsu.

To illustrate dangling bond passivation or, equivalently, the lack of defect states at the stoichiometric interface, the top panel of Figure 5c shows the inverse participation ratio (IPR), or equivalently electron localization calculated for each electronic state at the c-In_2O_3/a-MoO_3 interface near the bottom of the conduction and the top of the valence bands, respectively. These IPR values increase negligibly in comparison to a-MoO_3 bulk, suggesting that no strongly-localized tail states arise upon the interface formation. These calculations support the idea that any dangling bonds at the interface are passivated in the HSL structure. The corresponding density of states of Mo, O, and In states at the interface of HSL are plotted in Figure 5c lower panel. In the perfectly stoichiometric interface (i.e., with the Mo:O and In:O ratios being exactly 1:3 and 2:3), the empty Mo d-states that form the conduction band bottom are found to be about 0.5 eV lower with respect to the empty In s-states.

To further investigate the passivation of dangling bonds at the c-In_2O_3/a-MoO_3 interface, we also analyze the properties of deliberately sub-stoichiometric structures (Figure S5). For this, we calculate the formation energy of a single oxygen "vacancy" in either indium or molybdenum oxide layers at the interface. In structures with a negative formation energy of the defect (whereby oxygen sub-stoichiometry is likely), the

© 2023 The Authors. Advanced Materials published by Wiley-VCH GmbH

average Mo-O coordination is slightly above 3.7 and the lowest Mo-O coordination for an individual Mo is 3.06 (Figure S5, Supporting Information). Both values are nearly identical to those in bulk amorphous MoO_3, namely, 3.7 and 3.02, respectively, seen previously in Figure 5b. Comparing the band offsets between the molybdenum and indium oxide layers in the stoichiometric and sub-stoichiometric interfaces, the bottom of the conduction band for the crystalline In_2O_3 layer shifts downward with respect to the Mo *d*-states, which corresponds to the doping of the indium oxide layer, as expected from the lower In-O coordination in the sub-stoichiometric interface. Indeed, the calculated charge density distribution within the lowest conduction band reveals the charge localization between two pairs of severely under-coordinated In atoms (Figure S6.) This supports the interpretation that interfaces induce mild doping per the experimental data of Figure 4b, discussed previously.

2.6. Comparison to Original Tsu Superlattice

A word of discussion is in order regarding Tsu's own efforts and those of subsequent groups to create a semiconducting HSL in the *pc*-Si/*a*-SiO_2 system.[2] According to Tsu, an HSL structure should provide high mobility conduction if the dangling bonds at the *pc*/*a* interface are passivated, due to both the flexibility of bond angles in the amorphous phase and the presence of oxygen in the oxide for bond passivation. This proved difficult in Tsu's own attempts, where the oxygen from the *a*-SiO_2 passivation appeared to diffuse through the entire Si layer in some places, resulting in layers of Si quantum dots in a SiO_2 matrix.[2] And in follow-up studies by other researchers where a layered structure was preserved, the charge traps appear to have rendered the superlattices completely insulating.[21,22,23] In the latter case, this is likely because the bond angles in *a*-SiO_2 were insufficiently flexible to overcome the overly rigid tetragonal bond angles of the *pc*-Si, resulting in a high density of unpassivated dangling bonds and therefore trapped charge. By contrast, the *pc*-In_2O_3 investigated here has an amorphous-to-crystalline phase transition near room temperature, so the redirection of bond angles is not energetically expensive, and the *pc*-In_2O_3/*a*-MoO_3 oxide-to-oxide interface has a ready supply of oxygen for passivation of dangling bonds at the interface. The result is a mobility that rivals the best amorphous In_2O_3 layers grown.[16]

3. Conclusion

An unconventional multi-morphology approach is adopted to realize an HSL structure, which sandwiches thin polycrystalline layers of one material between similarly thin amorphous layers of another material. The complementary morphologies in each lattice period appear to greatly suppress interface defects as predicted by Tsu, permitting semiconducting layers to maintain doping levels consistent with bulk doping. Simultaneously, the interleaved amorphous layers appear to significantly enhance the electron mobility of the polycrystalline layer, suggesting an optimal layer thickness at 7 nm per layer. The low strain observed in XRD and high quality of the charge transport implies that strain and cumulative defects in the polycrystalline In_2O_3 are suppressed with each repeating amorphous layer, and that this defect suppression can continue to an HSL of arbitrary thickness. MD simulations suggest that dangling bonds at the interface are suppressed by the first few layers of atoms in the polycrystalline layer adjacent to the amorphous interface.

By generalizing the superlattice concept beyond purely crystalline morphology, the heteromorphic structure realized here heralds mixed-morphology material combinations that can manifest novel materials properties. We point to challenges in the field of transparent semiconductors which might be met by such HSL structures. For example, increased mobility of transparent semiconductors can enhance switching speed or reduce power consumption in displays, and a modulation-doped HSL with additional doping inside the insulating MoO_3 layer should, in principle, increase the electron mobility for a given electron density, analogous to the originally proposed modulation-doped superlattice of Dingle, et al.[4] Or modulation doped HSLs could compensate for the heavy hole mass in *p*-type transparent conductors to realize higher mobilities there, as well. Finally, we note that HSLs introduce vertical device functionality such as HSL superlattice minibands or negative-differential resistance resonant-tunneling-diodes. Preliminary evidence from the authors indicates that phase coherent tunneling across multiple HSL periods can, in fact, be experimentally achieved.[39] This HSL concept should be realizable in other amorphous/polycrystalline material combinations where at least one of the layers has compliant bond angles, such as in compounds with an ionic bonding character.

4. Experimental Section

In this section, the experimental process, procedures, related equipment and the calculation details are described.

Thin Film Growth by PLD: It was emphasized that both *pc*-In_2O_3 and *a*-MoO_3 films were grown under identical growth conditions including identical growth temperature and identical ambient oxygen pressure. Oxide thin films were deposited by PLD with a 248 nm KrF excimer laser. The laser pulse duration was 25 ns and the pulse frequency was 2 Hz. Each pulse of 220 mJ was focused to 1 mm × 3 mm area at the target, which rotates at 5 rpm. *pc*-In_2O_3 and *a*-MoO_3 thin films were deposited from hot-pressed In_2O_3 and MoO_3 targets (25 mm diameter), respectively. Fused quartz substrates were mounted to the substrate holder with silver paste. The distance between the target and substrate was fixed to 10 cm. The chamber was pumped out before each deposition by the turbomolecular pump until the pressure reaches under 5×10^{-7} Torr. The flow of high-purity O_2 to the chamber was precisely controlled during deposition to obtain target oxygen pressure, and the temperature of the substrate was controlled by the electric resistive heated substrate holder. The optimal deposition pressure and temperature were 15 mTorr and 200 °C, respectively. Figure S1 (Supporting Information) shows the schematic diagram of the PLD system.

Characterization: Thin films were characterized using transmission electron microscopy (TEM, JEOL, JEM-2100F / JEM-ARM 300F) to investigate the cross-sectional morphology of the films, including thickness, crystal structure, and interface quality. TEM samples were prepared using a standard technique employing a focused ion beam (FIB, FEI, Helios Nanolab 600 dual-beam) microscope with Ga+ energy of 2 keV at 24 pA ion current. The surface morphology and cross-section

© 2023 The Authors. Advanced Materials published by Wiley-VCH GmbH

15214095, 0, Downloaded from https://onlinelibrary.wiley.com/doi/10.1002/adma.202207927 by Missouri University Of Science, Wiley Online Library on [17/04/2023]. See the Terms and Conditions (https://onlinelibrary.wiley.com/terms-and-conditions) on Wiley Online Library for rules of use; OA articles are governed by the applicable Creative Commons License

images of oxide films are analyzed by field emission scanning electron microscopy (FESEM, Hitachi, SU8030). The surface morphology and the root-mean-squared roughness are obtained by atomic force microscopy (AFM, Bruker, Dimension FastScan). The thickness of the films was measured by spectral reflectometer (Filmetrics, F20) and reconfirmed by stylus profilometer (Veeco, Dektak 150) and X-ray reflectivity (XRR) using Cu Kα X-ray source (Rigaku, Smartlab). The crystal structure of the film was analyzed by X-ray diffraction (XRD), and the thickness, density, and roughness were investigated by XRR. A 100 nm thick *pc*-In_2O_3 layer and a *a*-MoO_3 layer were deposited by PLD on separate quartz substrates to confirm the growth rate. Their measured thicknesses were consistent as measured with a stylus profilometer, XRR, and spectral reflectometer as shown in Figure S2 (Supporting Information). Carrier density, mobility, and resistivity of the oxide films at room temperature were obtained via the Van der Pauw method with a Hall effect measurement system (Ecopia, HMS-3000).

Calculations: Simulations of *a*-MoO_3 bulk structures were obtained using ab-initio molecular dynamics (MD) liquid-quench approach as implemented in the Vienna Ab Initio Simulation Package (VASP). The calculations were based on density functional theory (DFT) with periodic boundary conditions and employed the Perdew-Burke-Ernzerhof (PBE) functional within the projector augmented-wave method. For the simulation of the HSL interface, alternating layers of 68-atom amorphous MoO_3 and an 80-atom [100]-oriented crystalline In_2O_3 were constructed with periodic boundary conditions, creating two interfaces in one global crystallographic direction with infinite oxide planes along the other two directions. Five structures for *a*-MoO_3 bulk with the optimal density were employed for the simulation, resulting in five independent a-MoO_3/c-In_2O_3 interfacial models. The details of the theoretical approach method are described in Supporting Information.

Supporting Information

Supporting Information is available from the Wiley Online Library or from the author.

Acknowledgements

The authors acknowledge the support from NSF-DMREF grants DMR-1729779, DMR-1729016, and DMR-1842467. Computational resources were provided by NSF-MRI grant OAC-1919789.

Conflict of Interest

The authors declare no conflict of interest.

Author Contributions

W.L. designed and performed the overall experiment including sample preparation and analyses, X.C. perform sample preparations and electrical measurements, S.I.B. and S.K. analyzed the HRTEM and STEM. R.P.H.C. oversaw the experiments and conceived the original multilayer structure. J.M. performed the theoretical calculation. W.L., Q.S., D.S., M.B., V.D., J.B.K., and J.M. helped prepare the manuscript, and M.G. led the manuscript writing. All the authors reviewed the manuscript.

Data Availability Statement

The data that support the findings of this study are available from the corresponding author upon reasonable request.

Keywords

high mobility, indium oxide, MD simulations, superlattice, transparent conducting oxides

Received: August 30, 2022
Revised: February 26, 2023
Published online:

[1] L. Esaki, R. Tsu, *IBM J. Res. Dev.* **1970**, *14*, 61.
[2] R. Dingle, H. L. Stormer, A. C. Gossard, W. Wiegmann, *Appl. Phys. Lett.* **1978**, *33*, 665.
[3] C. Waschke, H. G. Roskos, R. Schwedler, K. Leo, H. Kurz, K. Köhler, *Phys. Rev. Lett.* **1993**, *70*, 3319.
[4] J. Faist, F. Capasso, D. L. Sivco, C. Sirtori, A. L. Hutchison, A. Y. Cho, *Science* **1994**, *264*, 553.
[5] A. Frano, E. Benckiser, Y. Lu, M. Wu, M. Castro-Colin, M. Reehuis, A. V. Boris, E. Detemple, W. Sigle, P. van Aken, G. Cristiani, G. Logvenov, H.-U. Habermeier, P. Wochner, B. Keimer, V. Hinkov, *Adv. Mater.* **2014**, *26*, 258.
[6] H. Y. Hwang, Y. Iwasa, M. Kawasaki, B. Keimer, N. Nagaosa, Y. Tokura, *Nat. Mater.* **2012**, *11*, 103.
[7] R. Tsu, E. H. Nicollian, A. Reisman, *Appl. Phys. Lett.* **1989**, *55*, 1897.
[8] L. J. Cui, U. D. Venkateswaran, B. A. Weinstein, F. A. Chambers, *Phys. Rev. B* **1989**, *45*, 9248.
[9] Q.-Y. Ye, R. Tsu, E. H. Nicollian, *Phys. Rev. B* **1991**, *44*, 1806.
[10] R. Tsu, US5216262A, **1993**.
[11] Y.-J. Seo, *Trans. Electric.l and Electronic Mat.* **2001**, *2*, 16.
[12] C.-G. Wang, R. Tsu, J. C. Lofgren, U.S.S.R. 6,376,337, **2002**.
[13] A. Descoeudres, L. Barraud, S. De Wolf, B. Strahm, D. Lachenal, C. Guérin, Z. C. Holman, F. Zicarelli, B. Demaurex, J. Seif, J. Holovsky, C. Ballif, *Appl. Phys. Lett.* **2011**, *99*, 123506.
[14] T. C. Chong, L. P. Shi, X. Q. Wei, R. Zhao, H. K. Lee, P. Yang, A. Y. Du, *Phys. Rev. Lett.* **2008**, *100*, 136101.
[15] D. J. Eaglesham, J. M. Poate, D. C. Jacobson, M. Cerullo, L. N. Pfeiffer, K. West, *Appl. Phys. Lett.* **1991**, *58*, 523.
[16] R. W. Fathauer, T. George, E. W. Jones, W. T. Pike, A. Ksendzov, R. P. Vasquez, *Appl. Phys. Lett.* **1992**, *61*, 2350.
[17] S. Miyazaki, Y. Ihara, M. Hirose, *J. Non-Cryst. Solids* **1987**, *97–98*, 887.
[18] M. Zacharias, J. Bläsing, P. Veit, L. Tsybeskov, K. Hirschman, P. M. Fauchet, *Appl. Phys. Lett.* **1999**, *74*, 2614.
[19] M. Zacharias, J. Bläsing, K. Hirschman, L. Tsybeskov, P. M. Fauchet, *J. Non-Cryst. Solids* **2000**, *266–269*, 640.
[20] C. Deneke, R. Songmuang, N. Y. Jin-Phillipp, O. G. Schmidt, *J. Phys. D: Appl. Phys.* **2009**, *42*, 103001.
[21] W.-B. Zhang, Q. Qu, K. Lai, *ACS Appl. Mater. Interfaces* **2017**, *9*, 1702.
[22] M. Davide, L. Henrik, B. Arumugam Chandra, O. Kostya, *Nanotechnology* **2008**, *19*, 495302.
[23] F. Ji, X. Ren, X. Zheng, Y. Liu, L. Pang, J. Jiang, S. (F.) Liu, *Nanoscale* **2016**, *8*, 8696.
[24] R. Dingle, H. L. Stormer, W. Wiegmann, *Appl. Phys. Lett.* **1978**, *33*, 665.
[25] K. Inoue, T. Matsuno, *Phys. Rev. B* **1993**, *47*, 3771.
[26] T. C. L. G. Sollner, W. D. Goodhue, P. E. Tannenwald, C. D. Parker, D. D. Peck, *Appl. Phys. Lett.* **1983**, *43*, 588.
[27] E. E. Mendez, W. I. Wang, B. Ricco, L. Esaki, *Appl. Phys. Lett.* **1985**, *47*, 415.
[28] W. Walukiewicz, H. E. Ruda, J. Lagowski, H. C. Gatos, *Phys. Rev. B* **1984**, *30*, 4571.
[29] M. B. Zakaria, T. Nagata, A. Matsuda, Y. Yasuhara, A. Ogura, Md. S. A. Hossain, M. Billah, Y. Yamauchi, T. Chikyow, A. C. S. Appl, *Nano Mater* **2018**, *1*, 915.

© 2023 The Authors. Advanced Materials published by Wiley-VCH GmbH

15214095, 0, Downloaded from https://onlinelibrary.wiley.com/doi/10.1002/adma.202207927 by Missouri University Of Science, Wiley Online Library on [17/04/2023]. See the Terms and Conditions (https://onlinelibrary.wiley.com/terms-and-conditions) on Wiley Online Library for rules of use; OA articles are governed by the applicable Creative Commons License

[30] D. B. Buchholz, Q. Ma, D. Alducin, A. Ponce, M. Jose-Yacaman, R. Khanal, J. E. Medvedeva, R. P. H. Chang, *Chem. Mater.* **2014**, *26*, 5401.
[31] A. Nelson, *J. Appl. Crystallogr.* **2006**, *39*, 273.
[32] X.-L. Zhou, S.-H. Chen, *Phys. Rev. E* **1993**, *47*, 3174.
[33] X.-L. Zhou, *Phys. Rev. E: Stat. Phys., Plasmas, Fluids, Relat. Interdiscip. Top.* **1995**, *52*, 1938.
[34] National Institute of Standards and Technology Center for Neutron Research, https://www.ncnr.nist.gov/resources/activation/ (accessed: March 2023).
[35] C.-C. Yu, K.-S. Yang, H. Chang, J.-S. Lee, J.-Y. Lai, P.-Y. Chuang, J.-C. A. Huang, A.-C. Sun, F.-C. Wu, H.-L. Cheng, *Vacuum* **2014**, *102*, 63.
[36] Y. Saito, C. Kaito, T. Naiki, *J. Cryst. Growth* **1986**, *79*, 436.
[37] A. Mazor, D. J. Srolovitz, P. S. Hagan, B. G. Bukiet, *Phys. Rev. Lett.* **1988**, *60*, 424.
[38] G. K. Williamson, W. H. Hall, *Acta Metall.* **1953**, *1*, 22.
[39] Q. Shao, C. C. Aygen, X. Chen, W. Lee, R. P. H. Chang, J. E. Medvedeva, M. A. Grayson, unpublished.

© 2023 The Authors. Advanced Materials published by Wiley-VCH GmbH

15214095, 0, Downloaded from https://onlinelibrary.wiley.com/doi/10.1002/adma.202207927 by Missouri University Of Science, Wiley Online Library on [17/04/2023]. See the Terms and Conditions (https://onlinelibrary.wiley.com/terms-and-conditions) on Wiley Online Library for rules of use; OA articles are governed by the applicable Creative Commons License